Diamond-based multi electrode arrays for monitoring neurotransmitter release

Noname manuscript No.
(will be inserted by the editor)

Diamond-Based Multi Electrode Arrays for Monitoring Neurotransmitter Release

Giulia Tomagra · Alfio Battiato · Ettore Bernardi · Alberto Pasquarelli · Emilio Carbone · Paolo Olivero · Valentina Carabelli and Federico Picollo

Received: date / Accepted: date

Abstract In the present work, we report on the fabrication of a diamond-based device targeted to the detection of quantal neurotransmitter release. We have developed Multi-Electrode Arrays with 16 independent graphitic channels fabricated by means of Deep Ion Beam Lithography (DIBL). These devices are capable of detecting the *in vitro* exocytotic event from neurosecretory cells, while overcoming several critical limitations of standard amperometric techniques.

Keywords Diamond-based sensor · electrochemical detection · neuronal network · Ion beam lithography

1 Introduction

Exocytosis is a key process of synaptic transmission that occurs when the presynaptic terminal of a neuron is depolarized by an upcoming action potential. Presynaptic Ca^{2+} channels open and the Ca^{2+} flowing into the nerve terminal triggers the exocytosis of presynaptic vesicles. The released neurotransmitters diffuse into the synaptic cleft from the presynaptic terminal to the inter-synaptic space and activate the post-synaptic receptors of neighbouring neurons [1]. Charged oxidizable molecules released from single excitable cells are commonly detected using amperometry, an electrochemical technique that allows resolving the kinetics of fusion and opening of single secretory vesicles with high temporal resolution [2,3].
Currently, carbon fiber electrodes are conventionally employed for amperometric measurements of neurotransmitters release, but this technique has some limitations: i) its complexity requires trained operators; ii) it needs long

Giulia Tomagra
Corso Raffaello 30. Torino, 10125
Tel.: 0116708312
Fax: 0116708498 E-mail: gtomagra@unito.it

acquisition times in (single-cell measurements) and iii) detects only oxidizable molecules. Recently, planar multielectrode devices have been developed to overcome these limitations by exploiting several materials: indium, tin oxide (ITO) diamond-like carbon (DLC), boron-doped nanocrystalline diamond, noble metals (Au, Pt) and silicon-based chips[4].
A new promising substrate for cellular biosensors realization is diamond, that offers a wide spectrum of properties such as an excellent optical transparency, from infrared to near-ultraviolet [5], chemical inertness [6], biocompatibility [7],[8] and the possibility of tuning its electrical properties by directly writing sub-superficial electrodes by MeV ionic lithography [9]-[12].
In this paper, we describe the microfabrication of monocrystalline diamond substrates for the realization of microelectrode array cellular sensors based on graphitic micro channels (μG-SCD MEA).

2 μG-SCD MEA microfabrication

Ion beam lithography in diamond is a widely explored technique, which was employed to realize several structures [13]-[15] and devices, such as waveguides [16], [17] micromechanical resonator [18], [19], photonic structure [20], [21] particle detectors [22]-[25] and microfluidic channels [26], [27].
This technique exploits the metastable nature of the diamond by giving access to properties of various carbon allotropes, which are completely different (i.e. diamond is an optically transparent electrical insulator, while the graphite is an opaque conductor).
MeV collimated ions are employed to introduce structural damage within the diamond lattice, by inducing the formation of vacancies that promote the progressive creation of a network of sp3- and sp2-bonded carbon atoms. Above a critical level which is usually called graphitization threshold ($1 \times 10^{22} \div 9 \times 10^{22} cm^{-3}$ [28]-[30]), the complete amorphization of the irradiated material is reached and therefore a high temperature thermal annealing ($> 900°C$) results in the conversion to graphite is obtained. This phenomenon allows the formation of electrically conductive graphitic paths embedded in an insulating diamond matrix.
The employed diamond substrates are typically single crystals with dimensions of $4.5 \times 4.5 \times 0.5\ mm^3$, cut along the (100) crystalline direction and optically polished on the two opposite large faces. The crystals are classified as type IIa, with nitrogen and boron concentrations lower than 1 ppm and 0.05 ppm, respectively. Ion irradiation was performed at room temperature with a broad beam of light ions (i.e. He) with energy comprised between 0.5 MeV and 2 MeV at the INFN National Laboratories of Legnaro, facility equipped with linear accelerator employed for multidisciplinary experiments [31], [32]. The implantation fluence must be defined in order to overcome the critical damage density in correspondence of the Bragg peak[33].
Monte Carlo simulations performed with SRIM code [34] allow evaluating the ion-induced to structural damage on the basis of specific irradiation parame-

ters. For example, *figure 1* shows that an implantation fluence of $1 \times 10^{17} cm^{-2}$ is sufficient to amorphize the diamond with a 2 MeV He beam.

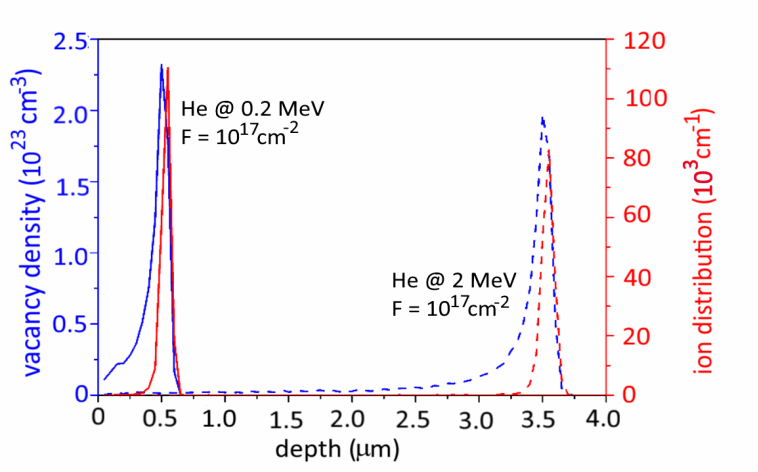

Fig. 1 SRIM Monte Carlo simulation: graphitization threshold is reported in dashed line, the zone of interest is in correspondence of the intersection of the Bragg peak, with the correspondence threshold.

The implantations are performed employing two high-resolution masks that define the 3D geometry of the graphitic structures. The first mask is made up of a metal sheet on which apertures are created through high power laser ablation and it is employed to block the ion beam with the exception of the aperture thus defines the length and width of the graphitic channels. The second mask consists of a metal film deposited directly on the diamond surface by means of thermal evaporation allowing the beam energy modulation that affects the penetration depth. This is functional to connect the buried structures with the sample surface.

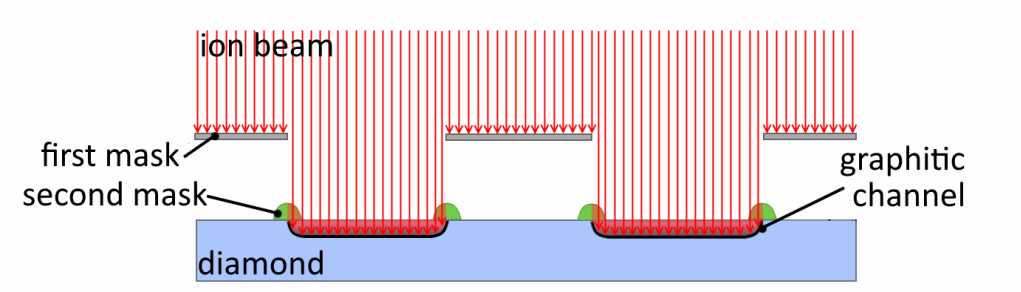

Fig. 2 Deep ion beam lithography of synthetic diamond.

With these masks, it is possible to implant simultaneously an array of 16 graphitic channels, whose end-points are exposed to the surface acting as multiple bio-sensing electrodes for *in vitro* cellular recordings [35], [36].
After implantation, high temperatures treatment is performed ($> 950°$) in high vacuum ($\sim 10^{-6} mbar$) for 2 hours in order to induce the permanent conversion of the amorphized regions to a graphite-like phase. 16 graphitic micro-channels (width: $\sim 20\mu m$, length: $1.4 - 1.9mm$, thickness:$\sim 250nm$) were obtained at a depth of few μm [37].
The graphitic channels are soldered by flip-chip technique to a polymer-ceramic composite chip carrier (Roger 4003) to allow the connection with the custom front-end electronics. The chip carrier is equipped with an incubation chamber that contains the culture medium necessary for *in vitro* experiments [38].
The front-end electronics consists of 16 low-noise transimpedance amplifiers with an input bias current of $\sim 2pA$ and a gain of 100, followed by Bessel low pass filters of the 6^{th}-order with a cut-off frequency of $1kHz$. The filtered signals are acquired with an ADC module (National Instrument USB-6229) having 16-bit resolution over an input range of $\pm 1V$ at a sampling rate up to $25kHz$ per channel. The data-acquisition module is interfaced with a PC through a Hi-speed USB link and controlled by a program developed in LabView environment [39].

3 Electrical Characterizations

I-V characteristics of the graphitic electrodes were measured to identify their conduction properties. *Figure 3* shows linear trends indicating that the electrodes have an ohmic conduction with resistances comprised between $5k\Omega$ and $9k\Omega$, which correspond to a resistivity of $\rho \sim 1.3m\Omega \cdot cm$, once the geometrical parameters are suitably taken into account. This value is in very satisfactory agreement with that of nanocrystalline graphite ($\rho \sim 1.3m\Omega \cdot cm$)[11], [40].

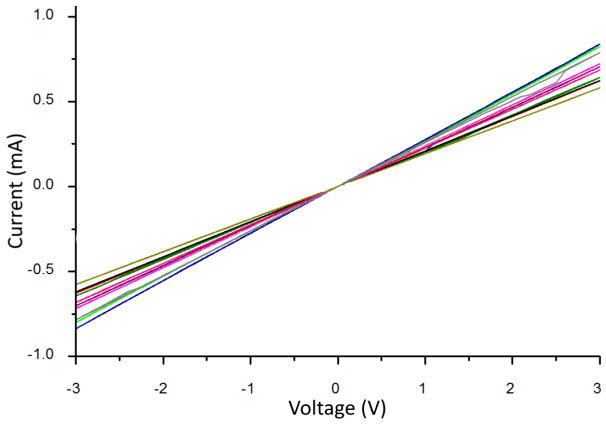

Fig. 3 Current-voltage characteristics of 16 graphitic electrodes.

In Electrochemical Impedance Spectroscopy measurements (EIS), a sinusoidal voltage of $10mV$ and variable frequency is applied, with the help of a potentiostat, between the working and the counter electrode and monitored by means of a reference electrode (3-electrode cell), thus measuring the total complex impedance of the circuit. EIS measurements were performed in a grounded Faraday cage to avoid external electric interferences, using a water-based electrolyte (PBS, phosphate buffer saline). The AC signal frequency varied between $0.1Hz$ and $100kHz$ with seven discrete points per decade, while the DC potential was kept constant at $0mV$.
Figure 4*a* and 4*b* reports the data of a representative channel. The module and phase of the impedance $\mid Z \mid$ as a function of the modulation frequent (*Bode plot*) were fitted using the equivalent circuit reported in *figure* 4*c*.

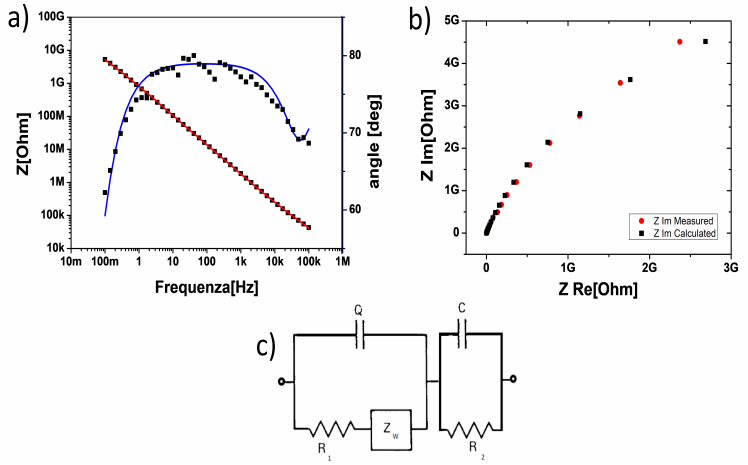

Fig. 4 Figure 4 a) Bode plot of a representative channel. The black squares represent the measured values, while the solid lines represent the fit considering the equivalent circuit reported in panel (c). b) Nyquist plot. The red circles represent the measured values, while the black squares represent the values calculated using the fit results. c) Equivalent circuit used to fit the experimental data. The first circuit mesh corresponds to a double layer imperfect capacitor Q, placed in parallel with the resistance due to charge transfer and the impedance due to the diffusion (the Warburg element Z_W). In addition to these elements, a second RC circuit (to the right) is considered to account for the bulk of the electrode.

Best-fit parameters were used to calculate the imaginary part of the impedance as function of the real part of the impedance and were compared with the experimental data, as shown in *figure 4b*, indicating good agreement between model and experimental data. The capacitance of the double layer (Q) resulting from the fit is consistent for all the channels (data not reported here) and his impedance is evaluated as $Z_Q = (3.1 \pm 1.2)\Omega$ assuming the pulse $\omega = 1$.
Cyclic voltammetry (see *Fig.5*) was performed to evaluate the sensitivity of μG-SCD MEA electrodes to detect dopamine. A physiological saline solutions, Tyrode solution, containing (in mM) 128 NaCl, 2 $MgCl_2$, 10 glucose,

10 HEPES, 10 $CaCl_2$ and 4 KCl (pH 7.4), and a Tyrode solution containing dopamine at different concentrations (25 and 100μM), were employed in these tests. A triangular voltage waveform, ranging from -0.5 V and $+1.1$ V, and with $20mVs^{-1}$ scan rate was applied to the graphitic electrodes.

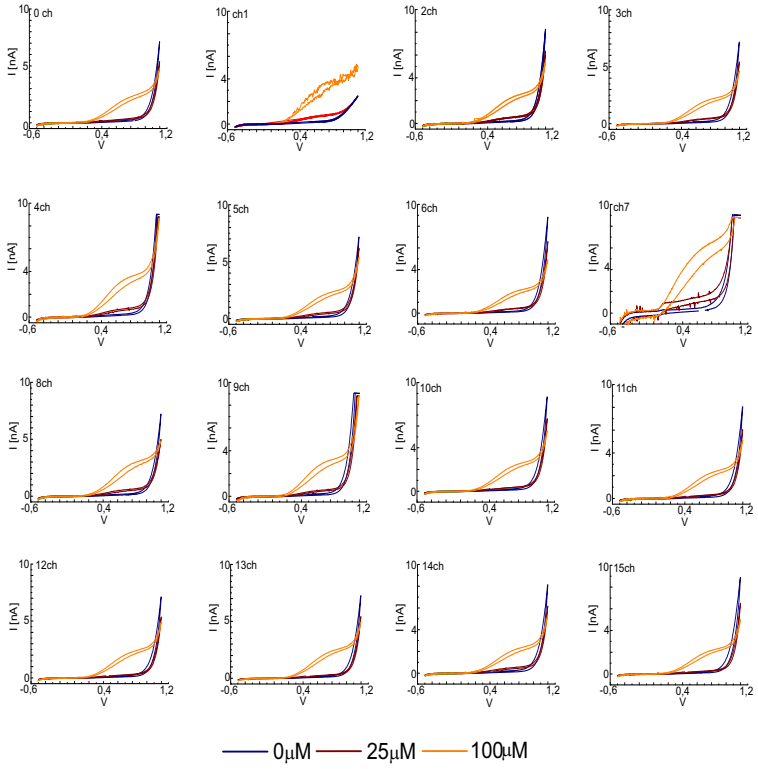

Fig. 5 Steady-state ciclic voltammograms of tyrode in control ($0\mu M$) and with dopamine solution at different concentration ($25, 100\ \mu M$).

The solution was grounded with a quasi-reference Ag/AgCl electrode. No redox activity was observed using the Tyrode solution in the anodic interval of the hydrolysis window, i.e. up to a polarization voltage of $+0.9$ V. Under these conditions, a leakage current of less than 10 pA was measured at $+0.6$ V.

The electrochemical window of the graphitic microelectrodes allowed the detection of the dopamine oxidation peak, between $+0.6$ V and $+0.8$ V [41], as shown in *Fig.5*.

4 Measurements of quantal dopamine release

Ca^{2+}-dependent neurotransmitter release from presynaptic terminals is one of the main mechanisms regulating signal transmission between neurons. Its dysfunction is at the basis of various neurodegenerative diseases. Thus, any technical improvement that facilitates the study of synaptic activity is essential for better understanding the molecular basis of neurosecretion.
Currently, the technique conventionally used to study catecholamine secretion is the amperometric recording with carbon fiber electrodes (CFE). This approach allows the study of quantal release associated to each single quantal event using a redox reaction mechanism between the secreted substance and the carbon fiber. This technique is limited to the measurement of a single cell at a time.

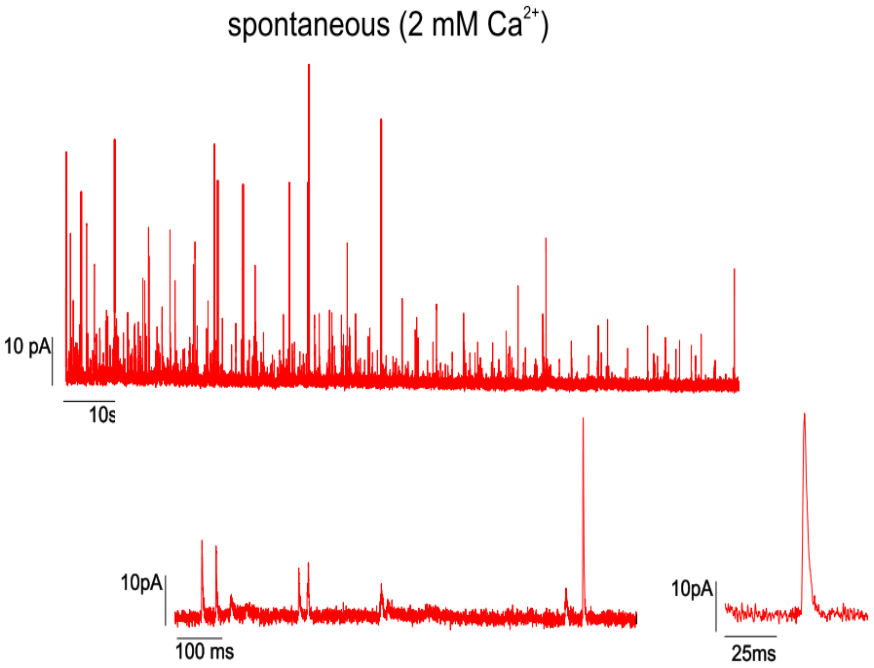

Fig. 6 An example of amperometric recording from PC12 cells.

The μG-SCD MEA overcome these limitations recording by simultaneously recording amperometric spikes from more cells, up to 16, maintaining the same high sensitivity and submillisecond temporal resolution of CFEs [42]-[44]. *Fig.* 6 shows an amperometric recording from an exemplifying electrode. The amperometric signals are collected for 120 s at a sampling rate of 25 kHz. Each spike represents the amperometric current (oxidation) associated with the catecholamine (dopamine) content of a PC12 cells, plated and cultured on

the μG-SCD MEA.
PC12 cells are a cell-line derived from rat pheochromocytoma of the adrenal medulla, used as a model of dopaminergic neurosecretory cell.

5 Conclusion

In the present paper, we have described the fabrication of diamond-based multi-electrode array for *in vitro* measurements of quantal neurotransmitter release. The presented technique allowed the microfabrication of graphitic channels that act as sensing microelectrodes embedded into a single-crystal diamond matrix. An extensive electrical characterization of these electrodes and typical recordings obtained with the MEA μG-SCD biosensor are reported.

Acknowledgements We thank G. Bruno for help in EIS measurement.

References

[1] T. C. Südhof, J. Rizo, T. C. Su, T. C. Südhof, and J. Rizo, Synaptic Vesicle Exocytosis, Cold Spring Harb. Perspect. Biol., vol. 3, no. 12, pp. 114, 2011.
[2] L. J. Mellander, R. Trouillon, M. I. Svensson, and A. G. Ewing, Amperometric post spike feet reveal most exocytosis is via extended kiss-and-run fusion, Sci. Rep., vol. 2, 2012.
[3] L. Simonsson, M. E. Kurczy, R. L. Trouillon, F. Hook, and A. S. Cans, A functioning artificial secretory cell, Sci. Rep., vol. 2, 2012.
[4] V. Carabelli et al., Planar Diamond-Based Multiarrays to Monitor Neurotransmitter Release and Action Potential Firing: New Perspectives in Cellular Neuroscience, ACS Chem. Neurosci., vol. 8, no. 2, pp. 252264, Feb. 2017.
[5] T. C. Granado et al., Progress in transparent diamond microelectrode arrays, Phys. status solidi, vol. 212, no. 11, pp. 24452453, Nov. 2015.
[6] R. J. Nemanich, J. A. Carlisle, A. Hirata, and K. Haenen, CVD diamondResearch, applications, and challenges, MRS Bull., vol. 39, no. 06, pp. 490494, 2014.
[7] P. Ariano et al., Cellular adhesion and neuronal excitability on functionalised diamond surfaces, Diam. Relat. Mater., vol. 14, no. 37, pp. 669674, 2005.
[8] P. Ariano, A. Lo Giudice, A. Marcantoni, E. Vittone, E. Carbone, and D. Lovisolo, A diamond-based biosensor for the recording of neuronal activity, Biosens. Bioelectron., vol. 24, no. 7, pp. 20462050, Mar. 2009.
[9] P. Olivero et al., Direct fabrication of three-dimensional buried conductive channels in single crystal diamond with ion microbeam induced graphitization, Diam. Relat. Mater., vol. 18, no. 58, pp. 870876, 2009.
[10] F. Picollo et al., Formation of buried conductive micro-channels in single crystal diamond with MeV C and He implantation, Diam. Relat. Mater., vol. 19, no. 56, pp. 466469, 2010.
[11] F. Picollo et al., Fabrication and electrical characterization of three-dimensional graphitic microchannels in single crystal diamond, New J. Phys., vol. 14, 2012.

[12] S. Prawer and R. Kalish, Ion-beam-induced transformation of diamond, Phys. Rev. B, vol. 51, no. 22, pp. 1571115722, 1995.
[13] F. Bosia et al., Finite element analysis of ion-implanted diamond surface swelling, Nucl. Instruments Methods Phys. Res. Sect. B Beam Interact. with Mater. Atoms, vol. 268, no. 19, pp. 29912995, Oct. 2010.
[14] F. Bosia et al., Modification of the structure of diamond with MeV ion implantation, Diam. Relat. Mater., vol. 20, no. 56, pp. 774778, May 2011.
[15] F. Bosia et al., Direct measurement and modelling of internal strains in ion-implanted diamond., J. Phys. Condens. Matter, vol. 25, no. 38, p. 385403, Sep. 2013.
[16] S. Lagomarsino et al., Evidence of light guiding in ion-implanted diamond, Phys. Rev. Lett., vol. 105, no. 23, p. 233903, Dec. 2010.
[17] S. Castelletto et al., Diamond-based structures to collect and guide light, New J. Phys., vol. 13, no. 2, p. 025020, Feb. 2011.
[18] M. Mohr et al., Characterization of the recovery of mechanical properties of ion-implanted diamond after thermal annealing, Diam. Relat. Mater., vol. 63, pp. 7579, 2016.
[19] J. Fu et al., Single crystal diamond cantilever for micro-electromechanical systems, Diam. Relat. Mater., vol. 73, pp. 267272, Mar. 2017.
[20] V. S. Drumm et al., Surface damage on diamond membranes fabricated by ion implantation and lift-off, Appl. Phys. Lett., vol. 98, no. 23, p. 231904, Jun. 2011.
[21] J. C. Lee, A. P. Magyar, D. O. Bracher, I. Aharonovich, and E. L. Hu, Fabrication of thin diamond membranes for photonic applications, Diam. Relat. Mater., vol. 33, pp. 4548, Mar. 2013.
[22] J. Forneris et al., A 3-dimensional interdigitated electrode geometry for the enhancement of charge collection efficiency in diamond detectors, EPL (Europhysics Lett., vol. 108, no. 1, p. 18001, 2014.
[23] J. Forneris et al., IBIC characterization of an ion-beam-micromachined multi-electrode diamond detector, Nucl. Instruments Methods Phys. Res. Sect. B Beam Interact. with Mater. Atoms, vol. 306, pp. 181185, 2013.
[24] P. Olivero et al., Focused ion beam fabrication and IBIC characterization of a diamond detector with buried electrodes, Nucl. Instruments Methods Phys. Res. Sect. B Beam Interact. with Mater. Atoms, vol. 269, no. 20, pp. 23402344, Oct. 2011.
[25] A. Lo Giudice et al., Lateral IBIC characterization of single crystal synthetic diamond detectors, Phys. Status Solidi - Rapid Res. Lett., vol. 5, no. 2, pp. 8082, Feb. 2011.
[26] F. Picollo et al., Fabrication of monolithic microfluidic channels in diamond with ion beam lithography, Nucl. Instruments Methods Phys. Res. Sect. B Beam Interact. with Mater. Atoms, vol. 404, pp. 193197, Aug. 2017.
[27] M. a. Strack et al., Buried picolitre fluidic channels in single-crystal diamond, SPIE Proc., vol. 8923, p. 89232X, Dec. 2013.
[28] D. P. Hickey, K. S. Jones, and R. G. Elliman, Amorphization and graphitization of single-crystal diamond - A transmission electron microscopy study, Diam. Relat. Mater., vol. 18, no. 11, pp. 13531359, 2009.

[29] A. Battiato et al., Softening the ultra-stiff: Controlled variation of Youngs modulus in single-crystal diamond by ion implantation, Acta Mater., vol. 116, pp. 95103, 2016.
[30] C. Uzan-Saguy, C. Cytermann, R. Brener, V. Richter, M. Shaanan, and R. Kalish, Damage threshold for ion-beam induced graphitization of diamond, Appl. Phys. Lett., vol. 67, p. 1194, 1995.
[31] V. Rigato, Interdisciplinary physics with small accelerators at LNL: Status and perspectives, 2013, pp. 2934.
[32] A. Re et al., Ion Beam Analysis for the provenance attribution of lapis lazuli used in glyptic art: The case of the Collezione Medicea, Nucl. Instruments Methods Phys. Res. Sect. B Beam Interact. with Mater. Atoms, vol. 348, pp. 278284, Apr. 2015.
[33] P. Olivero et al., Direct fabrication and IV characterization of sub-surface conductive channels in diamond with MeV ion implantation, Eur. Phys. J. B, vol. 75, no. 2, pp. 127132, Dec. 2010.
[34] J. F. Ziegler, M. D. Ziegler, and J. P. Biersack, SRIM - The stopping and range of ions in matter (2010), Nucl. Instruments Methods Phys. Res. Sect. B Beam Interact. with Mater. Atoms, vol. 268, no. 1112, pp. 18181823, 2010.
[35] F. Picollo et al., All-carbon multi-electrode array for real-time in vitro measurements of oxidizable neurotransmitters, Sci. Rep., vol. 6, 2016.
[36] F. Picollo et al., Realization of a diamond based high density multi electrode array by means of Deep Ion Beam Lithography, Nucl. Instruments Methods Phys. Res. Sect. B Beam Interact. with Mater. Atoms, vol. 348, pp. 199202, 2015.
[37] E. Bernardi, A. Battiato, P. Olivero, F. Picollo, and E. Vittone, Kelvin probe characterization of buried graphitic microchannels in single-crystal diamond, J. Appl. Phys., vol. 117, no. 2, 2015.
[38] E. Colombo et al., Fabrication of a NCD microelectrode array for amperometric detection with micrometer spatial resolution, Diam. Relat. Mater., vol. 20, no. 56, pp. 793797, 2011.
[39] F. Picollo et al., Development and Characterization of a Diamond-Insulated Graphitic Multi Electrode Array Realized with Ion Beam Lithography, Sensors, vol. 15, no. 1, pp. 515528, 2015.
[40] S. Ditalia Tchernij et al., Electrical characterization of a graphite-diamond-graphite junction fabricated by MeV carbon implantation, Diam. Relat. Mater., vol. 74, pp. 125131, 2017.
[41] S. Gosso et al., Heterogeneous distribution of exocytotic microdomains in adrenal chromaffin cells resolved by high-density diamond ultra-microelectrode arrays, J. Physiol., vol. 592, no. 15, pp. 32153230, 2014.
[42] F. Picollo et al., Microelectrode arrays of diamond-insulated graphitic channels for real-time detection of exocytotic events from cultured chromaffin cells and slices of adrenal glands., Anal. Chem., vol. 88, no. 15, pp. 74937499, 2016.
[43] F. Picollo et al., A new diamond biosensor with integrated graphitic microchannels for detecting quantal exocytic events from chromaffin cells, Adv. Mater., vol. 25, no. 34, pp. 46964700, Sep. 2013.

[44] V. Carabelli et al., Nanocrystalline diamond microelectrode arrays fabricated on sapphire techology for high-time resolution of quantal catecholamine secretion from chromaffin cells, Biosens. Bioelectron., vol. 26, no. 1, pp. 9298, 2010.